Supporting Information

Unbiased Photoelectrochemical Tandem Reaction for Concurrent Oxidations with Ultra-high Overall Faradaic Efficiency

Haoyue Sun,[a] *Rui Tang,*[a] *Xingmo Zhang,*[a] *Sibei Zou,*[a] *Yuhang Liang,*[a] *Namuersaihan Namuersaihan,*[a] *Qinfen Gu,*[c] *Alfons Baiker,*[b] *Jun Huang*[a]*

a. School of Chemical and Biomolecular Engineering, The University of Sydney, Sydney, NSW 2006 Australia.

b. Institute of Chemical and Bioengineering, Department of Chemistry and Applied Biosciences ETH Zurich, HCI, CH-8093 Zurich, Switzerland

c. Australian Synchrotron, ANSTO, 800 Blackburn Rd, Clayton, Victoria 3168, Australia

* Corresponding Author:

Prof. Jun Huang: jun.huang@sydney.edu.au

1. Supporting Figures

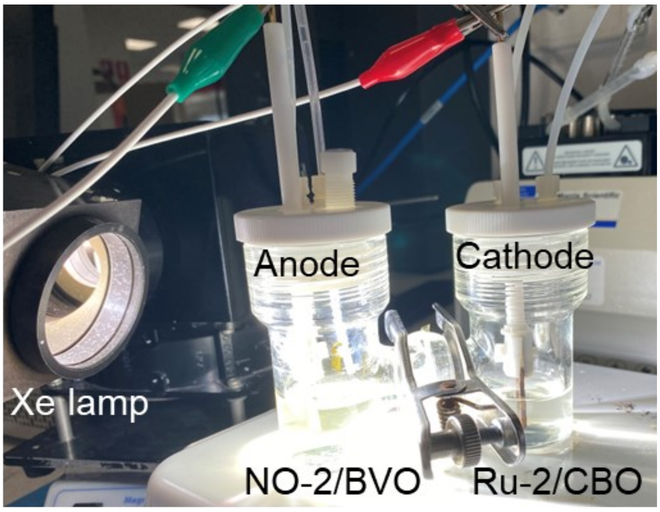

Figure S1. Photograph of tandem HMF oxidation device.

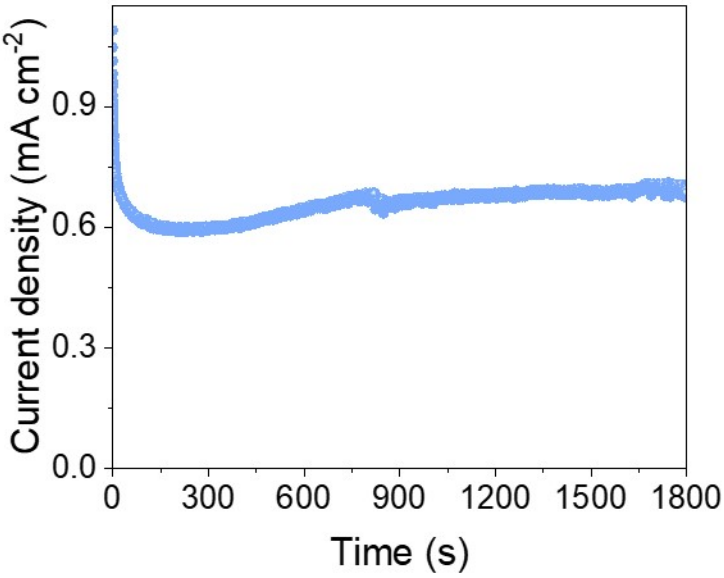

Figure S2. Long-term I–t curve of the tandem device.

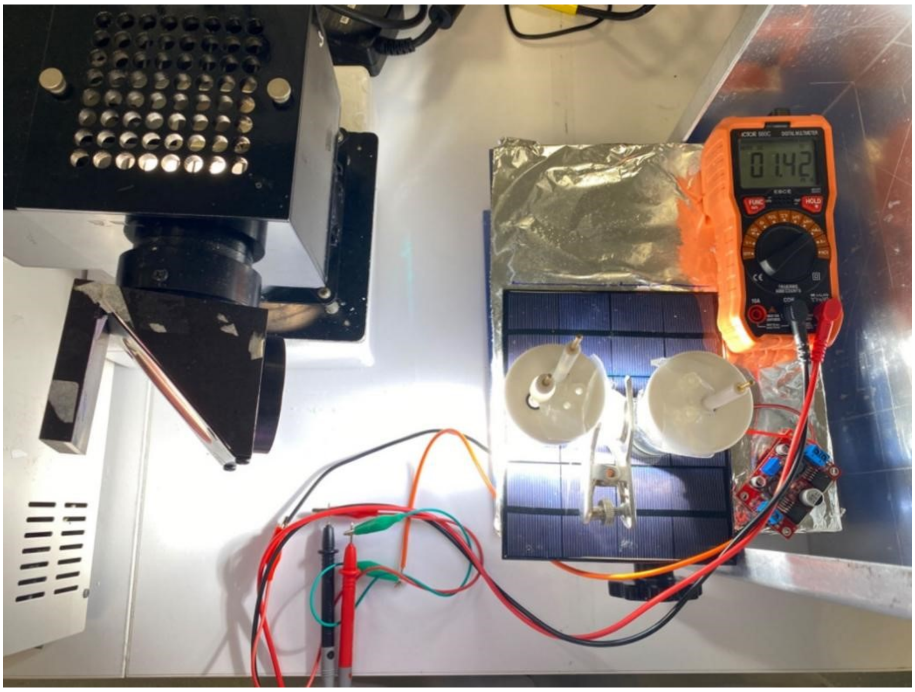

Figure S3. The corresponding current through the self-powered PEC HMF oxidation when using the 1.25 V solar panel.

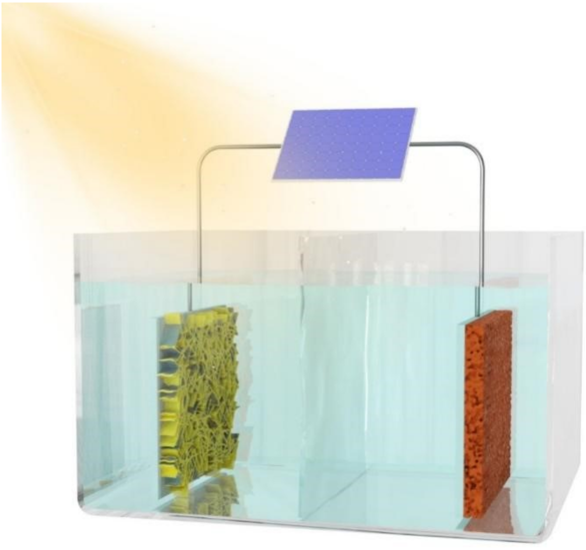

Figure S4. Schematic illustration of the self-powered PEC system equipped with a solar panel (~1.25 V) for HMF oxidation.

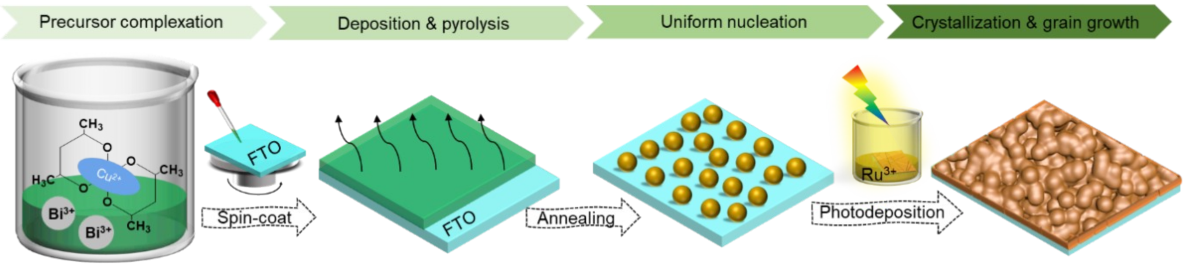

Figure S5. Synthesis scheme of Ru-*x*/CBO (*x*=1, 2 and 3).

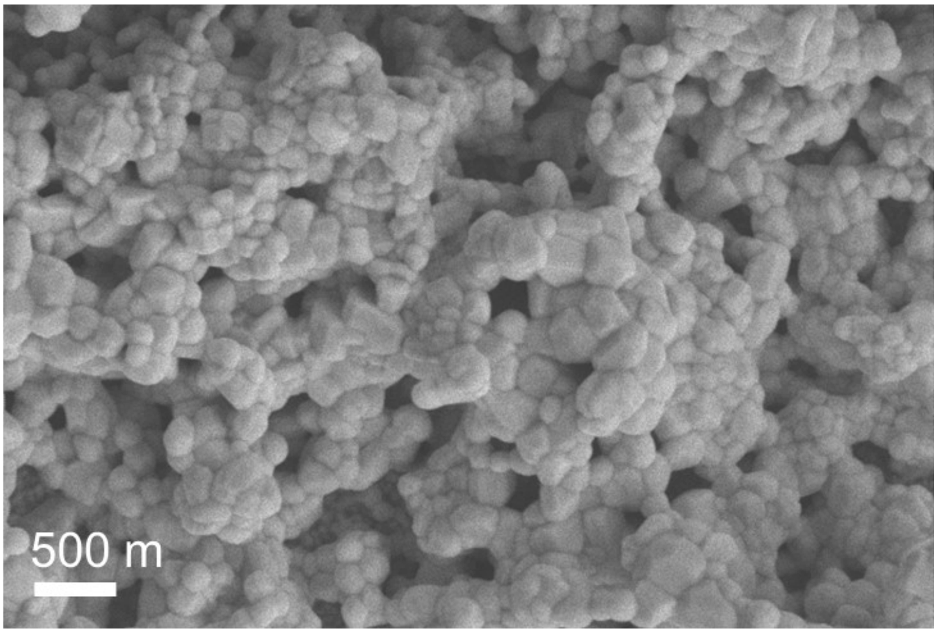

Figure S6. Top-view SEM image of CBO.

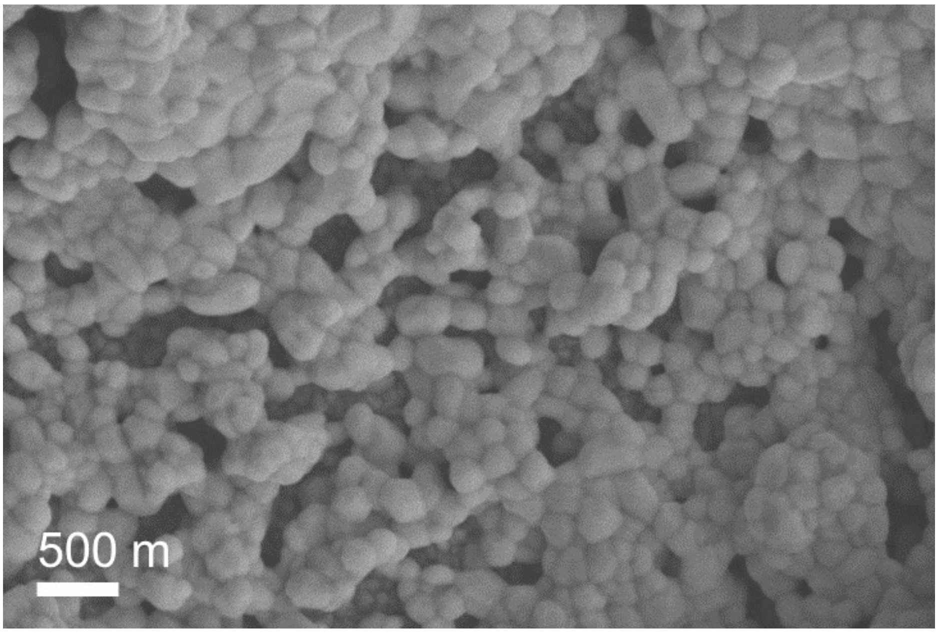

Figure S7. Top-view SEM image of Ru-1/CBO.

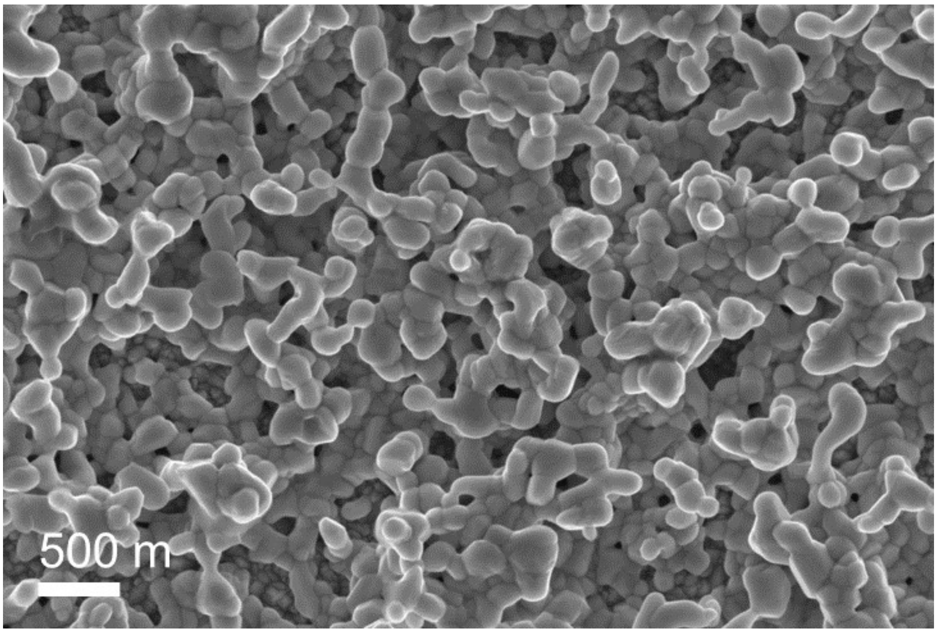

Figure S8. Top-view SEM image of Ru-3/CBO.

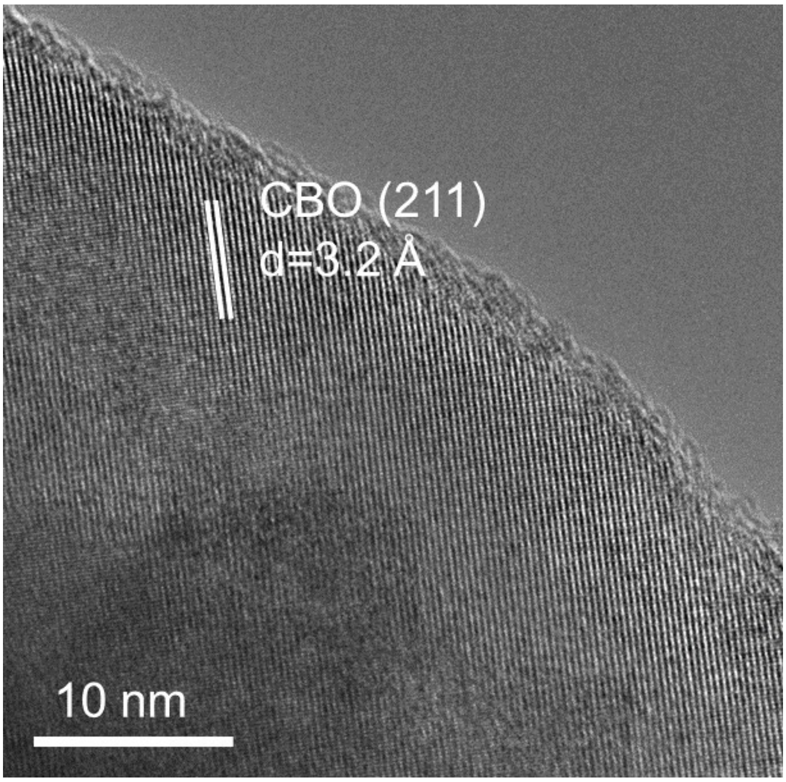

Figure S9. HR-TEM image of CBO.

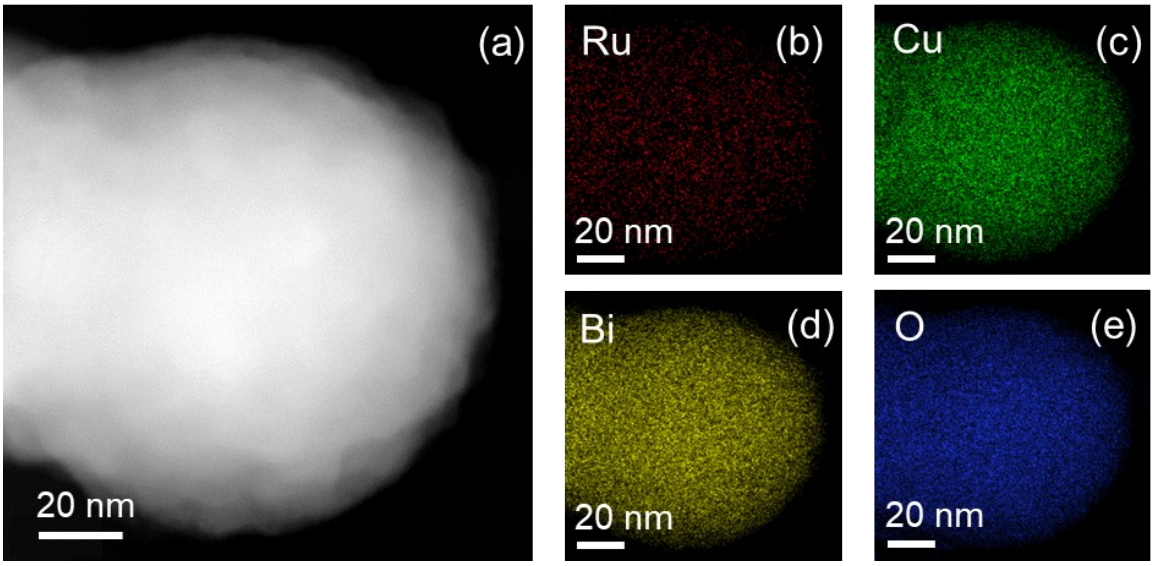

Figure S10. (a) HAADF image and (b-e) the corresponding EDS elemental mapping of Ru-2/CBO.

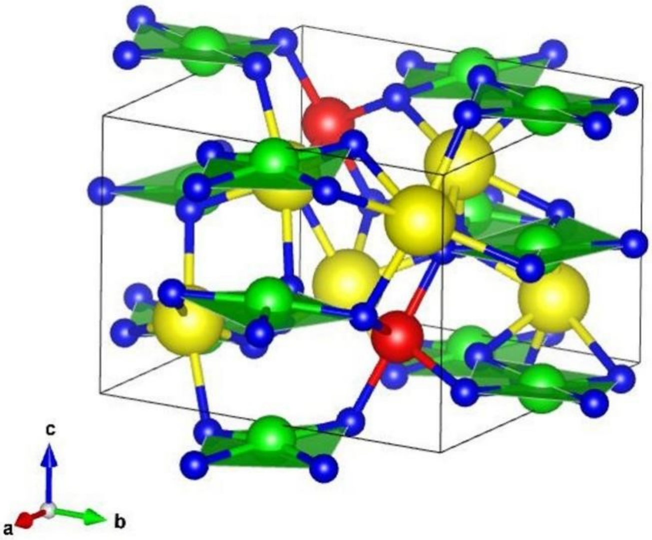

Figure S11. Formation of Ru-2/CBO by Ru replacing Bi. Red, green, yellow, and blue colored balls represent Ru, Cu, Bi, and O atoms, respectively.

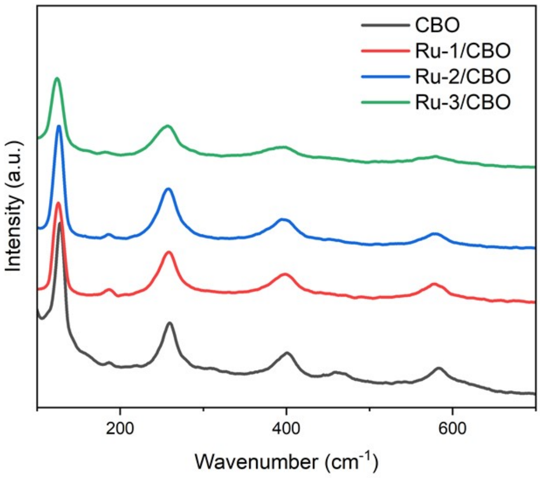

Figure S12. Raman spectra of the as-prepared Ru-*x*/CBO (*x*=1, 2, and 3) and CBO photocathodes.

CBO and Ru-*x*/CBO (*x* =1, 2, and 3) exhibit similar vibration peaks. The main peaks located at 132, 262, 403, and 588 cm^{-1} belong to CBO. Bands of Ru-*x*/CBO (*x* =1, 2, and 3) photocathodes are shifted to a lower wavenumber, indicating that Ru has been successfully doped into the host CBO.

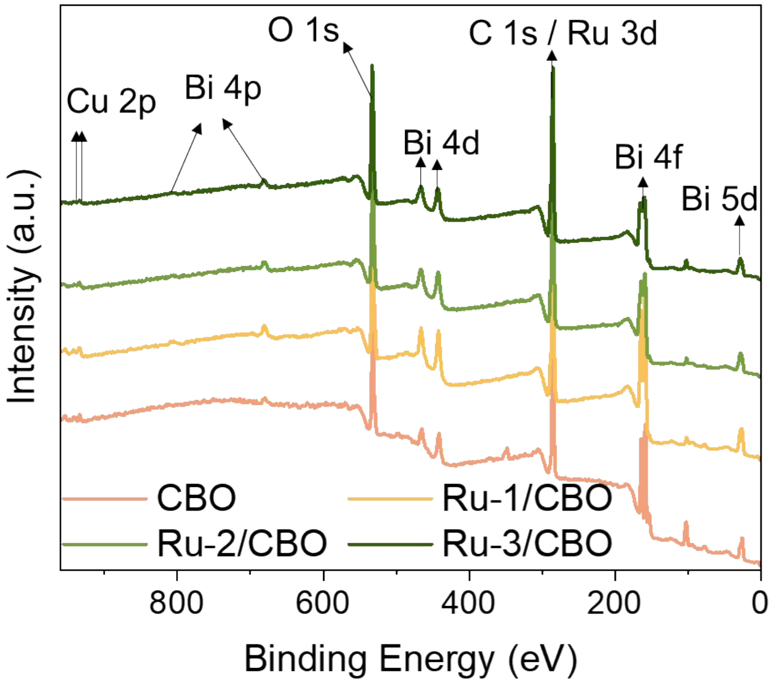

Figure S13. XPS survey spectra of Ru-*x*/CBO (*x* =1, 2, and 3) and CBO photocathodes.

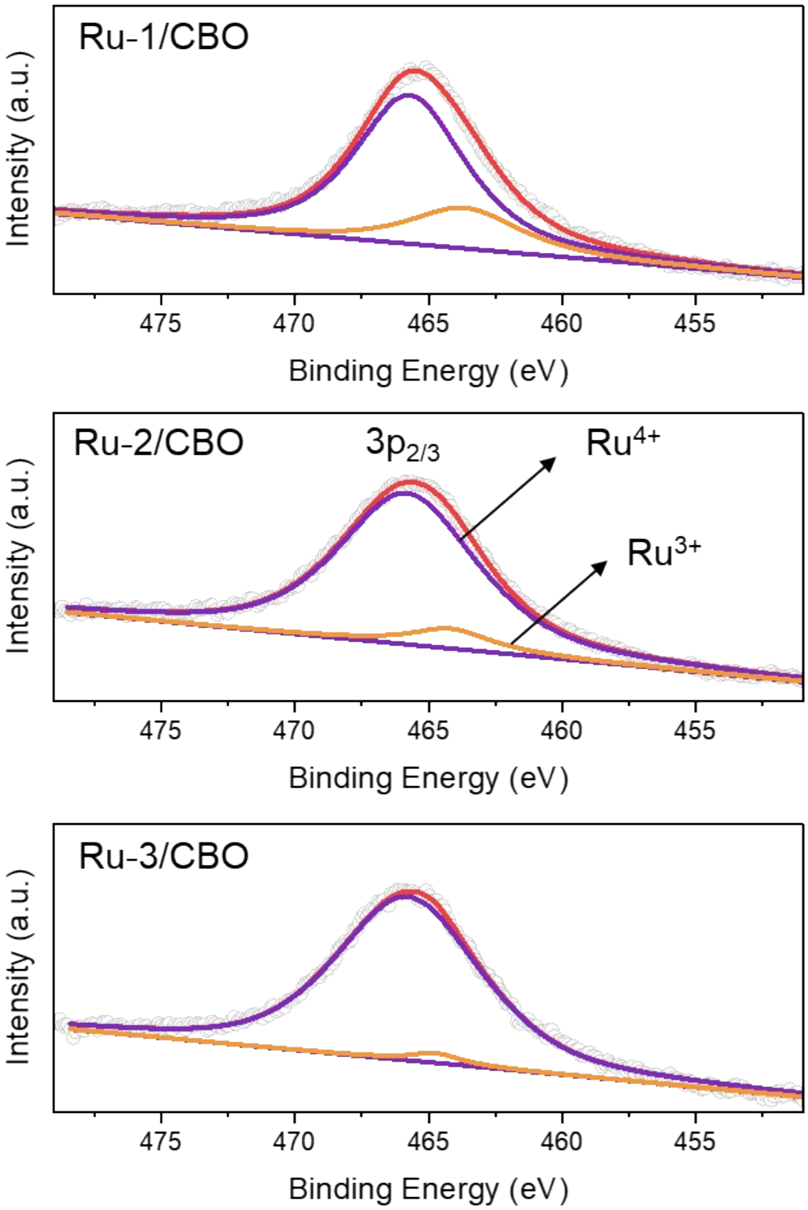

Figure S14. XPS spectra of Ru 3p peaks of (a) Ru-1/CBO and (b) Ru-3/CBO.

The Ru 3p peaks of Ru-2/CBO are well fitted into Ru^{3+} and Ru^{4+} species, according to the peaks at 464.1 and 465.9 eV in the Ru 3p XPS spectrum. A similar oxidation state of Ru is found in Ru-1/CBO and Ru-3/CBO.

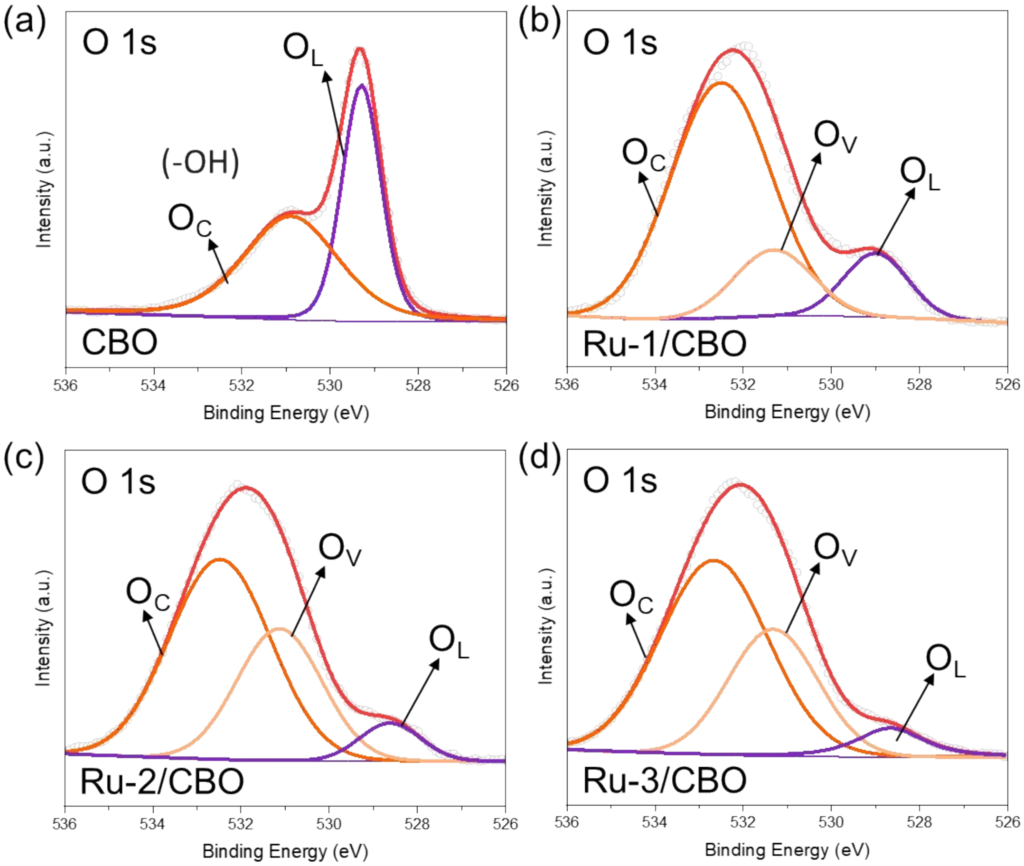

Figure S15. XPS spectra of O 1s peaks of (a) CBO, (b) Ru-1/CBO, (c) Ru-2/CBO, and (d) Ru-3/CBO.

Note that the O 1s spectra can be deconvoluted into two peaks at 530.0 and 532.2 eV, indicative of lattice and adsorbed oxygen (e.g., hydroxide). This is because CBO is prepared in a strong alkali environment.

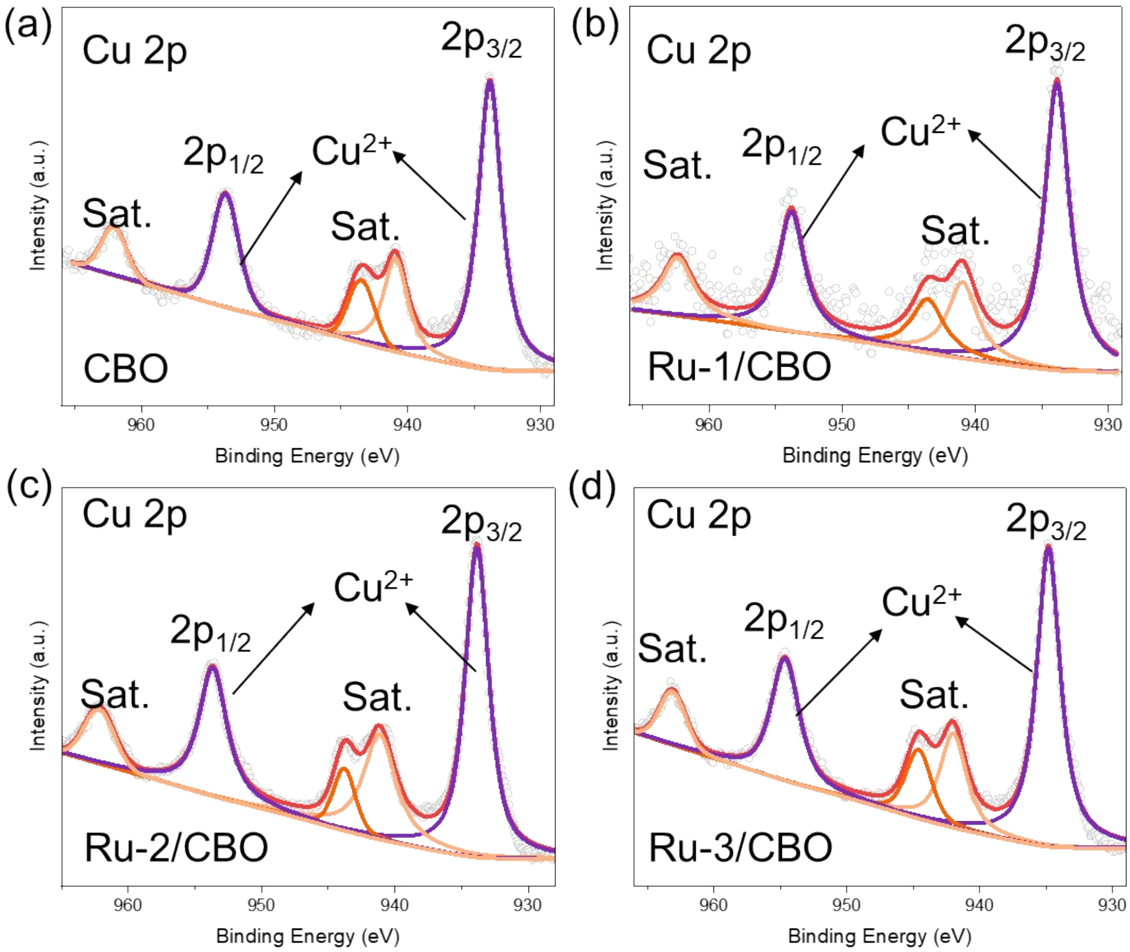

Figure S16. XPS spectra of Cu 2p peaks of (a) CBO, (b) Ru-1/CBO, (c) Ru-2/CBO, and (d) Ru-3/CBO.

The XPS spectra of the Cu 2p can be deconvoluted into five peaks. The peak located at 953.94 eV belongs to Cu 2p1/2, the two peaks, which appeared at 944.38 and 941.18 eV can be attributed to the shake-up satellites, while the peaks corresponding to Cu 2p3/2 are observed at 934.42 and 932.95 eV.[1]

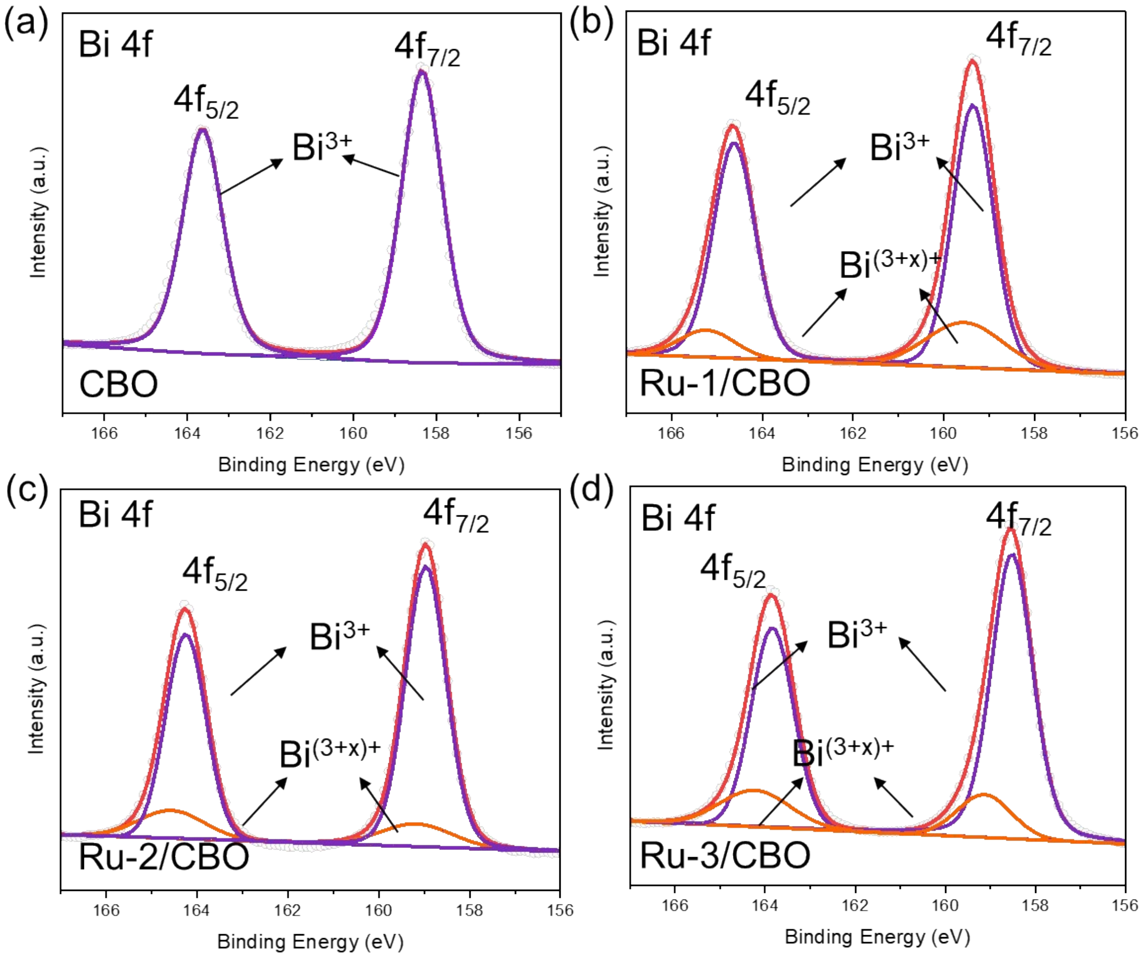

Figure S17. XPS spectra of Bi 4f peaks of (a) CBO, (b) Ru-1/CBO, (c) Ru-2/CBO, and (d) Ru-3/CBO.

In the Bi 4f spectra, the dominant peaks appear at 159.18 and 164.49 eV, confirming that Bi^{3+} is the main species in CBO. Two weak peaks located at high binding energy (160.46 and 165.72 eV) are observed in the Ru-2/CBO photocathode, corresponding to trace amounts of high-valence bismuth.

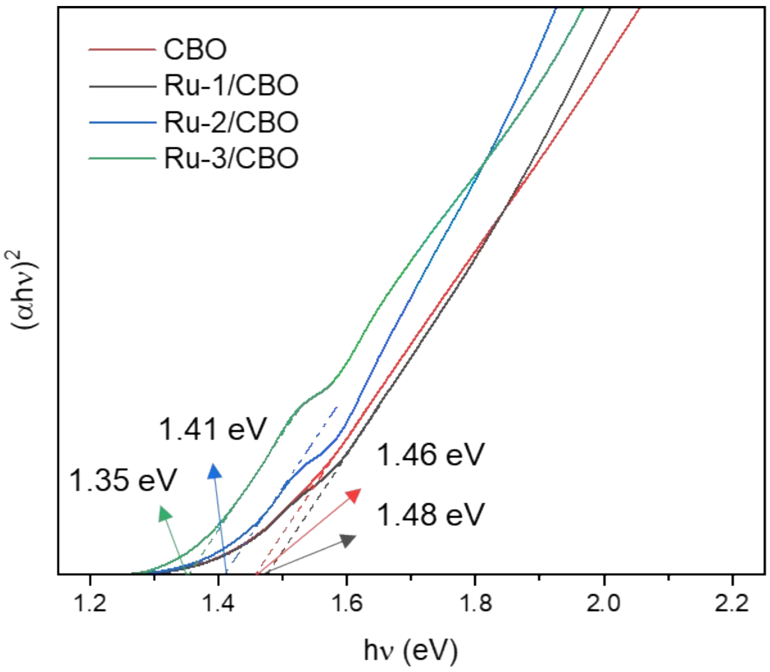

Figure S18. Tauc plots of CBO, Ru-1/CBO, Ru-2/CBO, and Ru-3/CBO.

According to the Kubelka-Munk function, the band gap energy (E_g) of CBO, Ru-1/CBO, Ru-2/CBO, and Ru-3/CBO was calculated to be 1.48, 1.46, 1.41 eV, and 1.35 eV, respectively. The reduced E_g value indicates that Ru doping in CBO can narrow the optical band gap and has a stronger ability to utilize visible light compared to pure CBO.

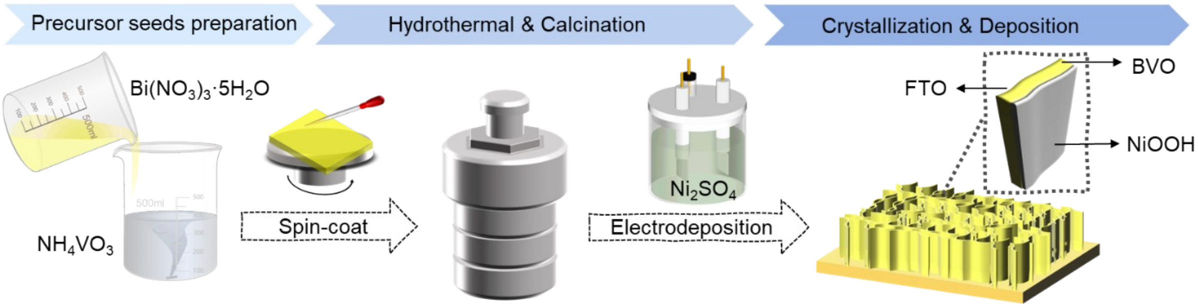

Figure S19. Synthesis scheme of NO-*x*/BVO (*x*=1, 2 and 3).

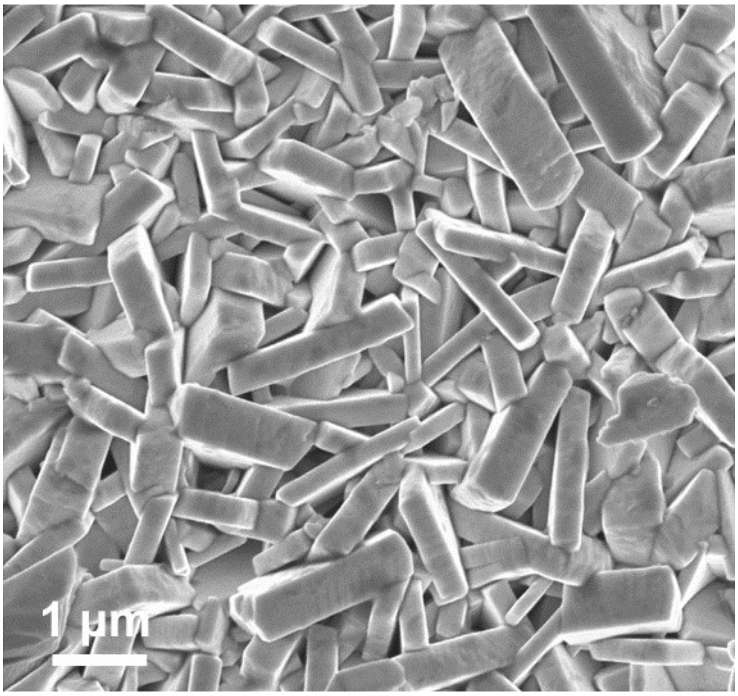

Figure S20. Top-view SEM image of BVO.

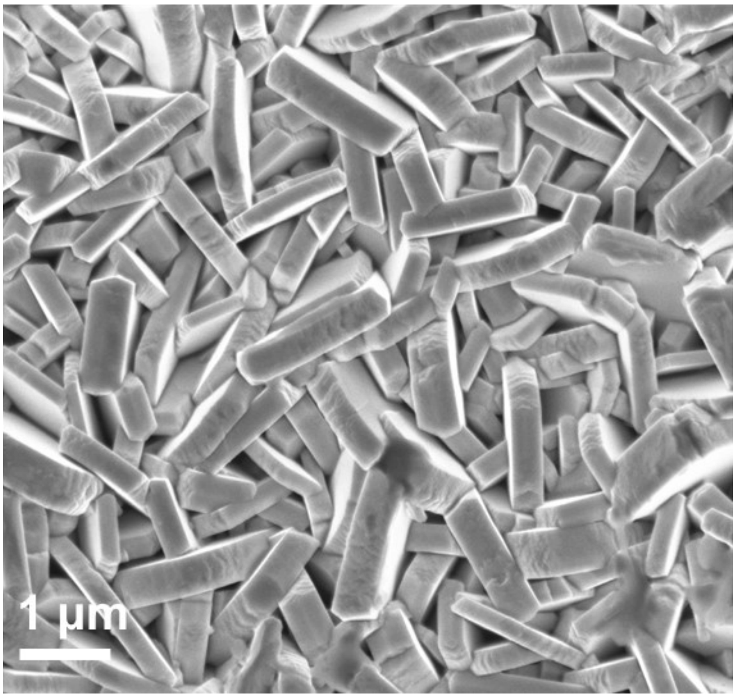

Figure S21. Top-view SEM image of NO-1/BVO.

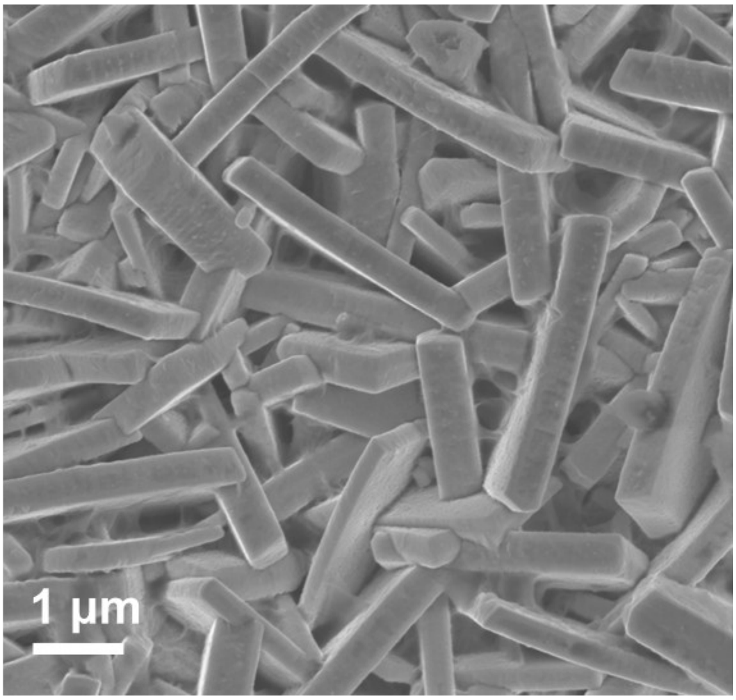

Figure S22. Top-view SEM image of NO-3/BVO.

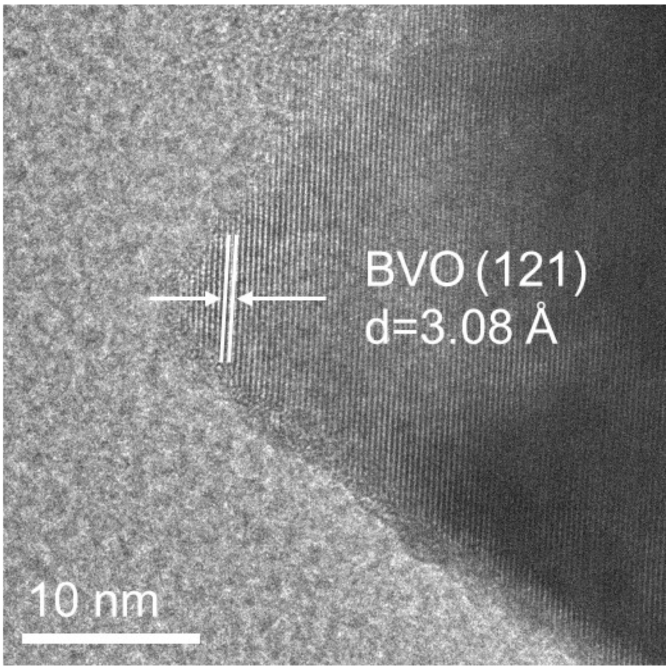

Figure S23. HR-TEM image of BVO.

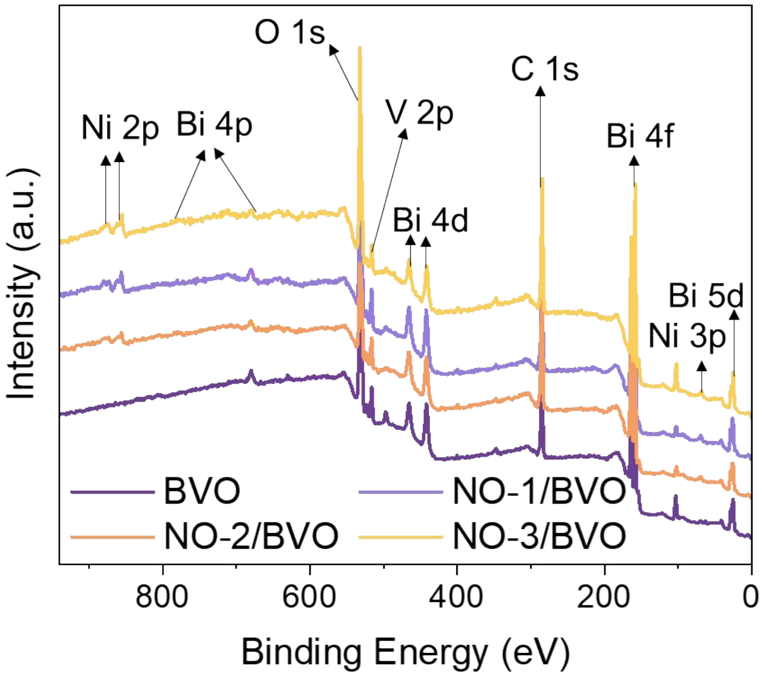

Figure S24. XPS survey spectra of (a) BVO, (b) NO-1/BVO, (c) NO-2/BVO, and (d) NO-3/BVO.

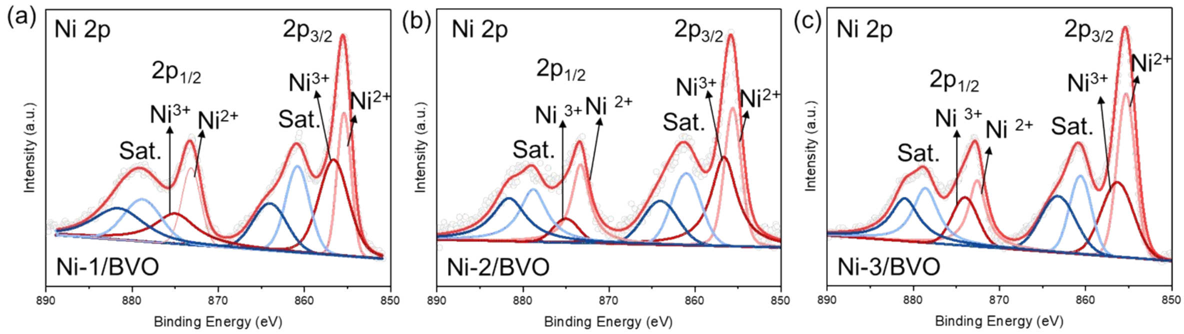

Figure S25. XPS spectra of Ni 2p peaks of (a) NO-1/BVO, (b) NO-2/BVO, and (c) NO-3/BVO.

The signals of Ni is detected in both NO-x/BVO photoanodes, the fitted peaks located at 855.5 eV (Ni^{2+} $2p_{3/2}$), 873.2 eV (Ni^{2+} $2p_{1/2}$), 856.0 eV (Ni^{3+} $2p_{3/2}$), and 875.7 eV (Ni^{3+} $2p_{1/2}$) indicate the presence of Ni^{2+} and Ni^{3+}, which supports the existence of NiOOH species.[2]

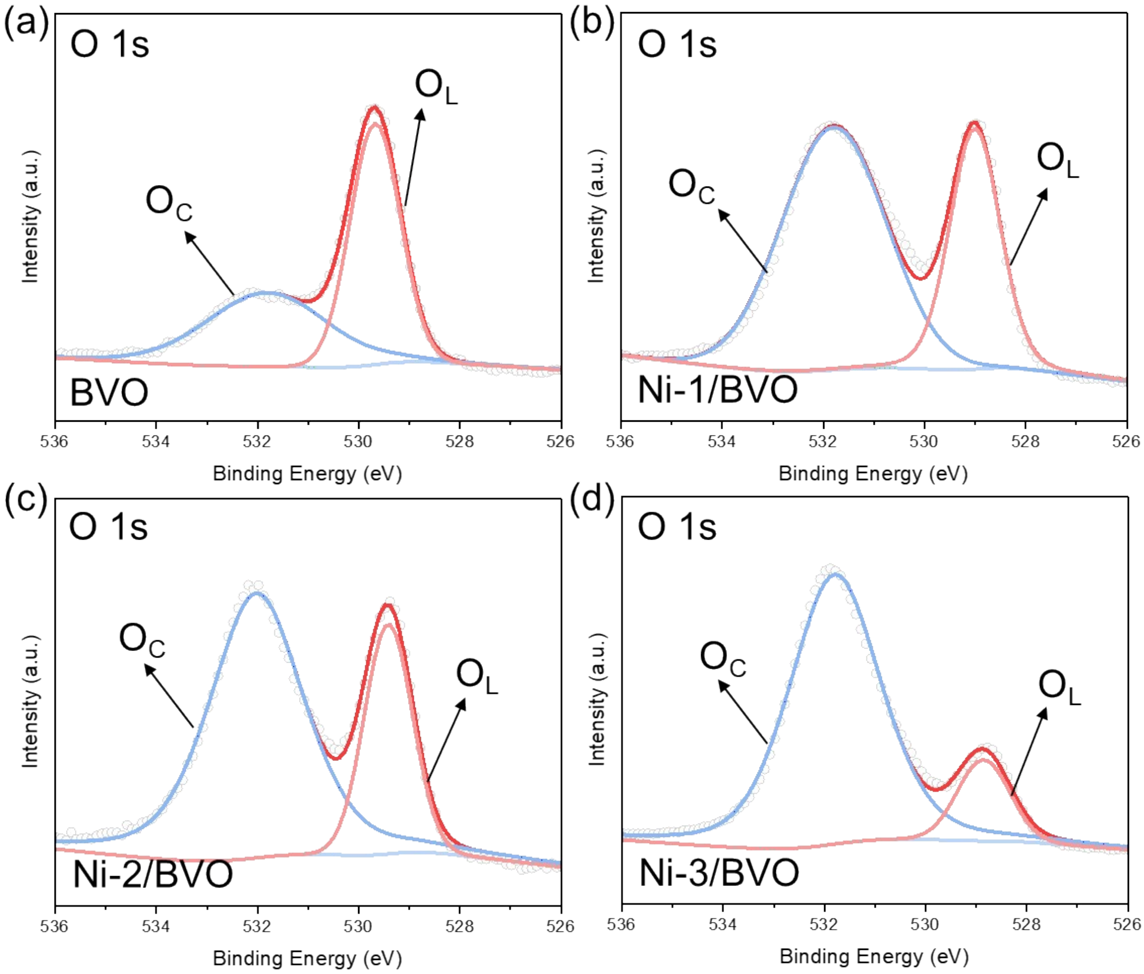

Figure S26. XPS spectra of O 1s peaks of (a) BVO, (b) NO-1/BVO, (c) NO-2/BVO, and (d) NO-3/BVO.

Deconvoluted peaks for high-resolution O 1 s spectra of photoanodes. The O 1 s spectra could be fitted into peaks at 529.6 eV and 531.8 eV, corresponding to lattice oxygen (O_L) and chemically absorbed oxygen (O_C), respectively.[3]

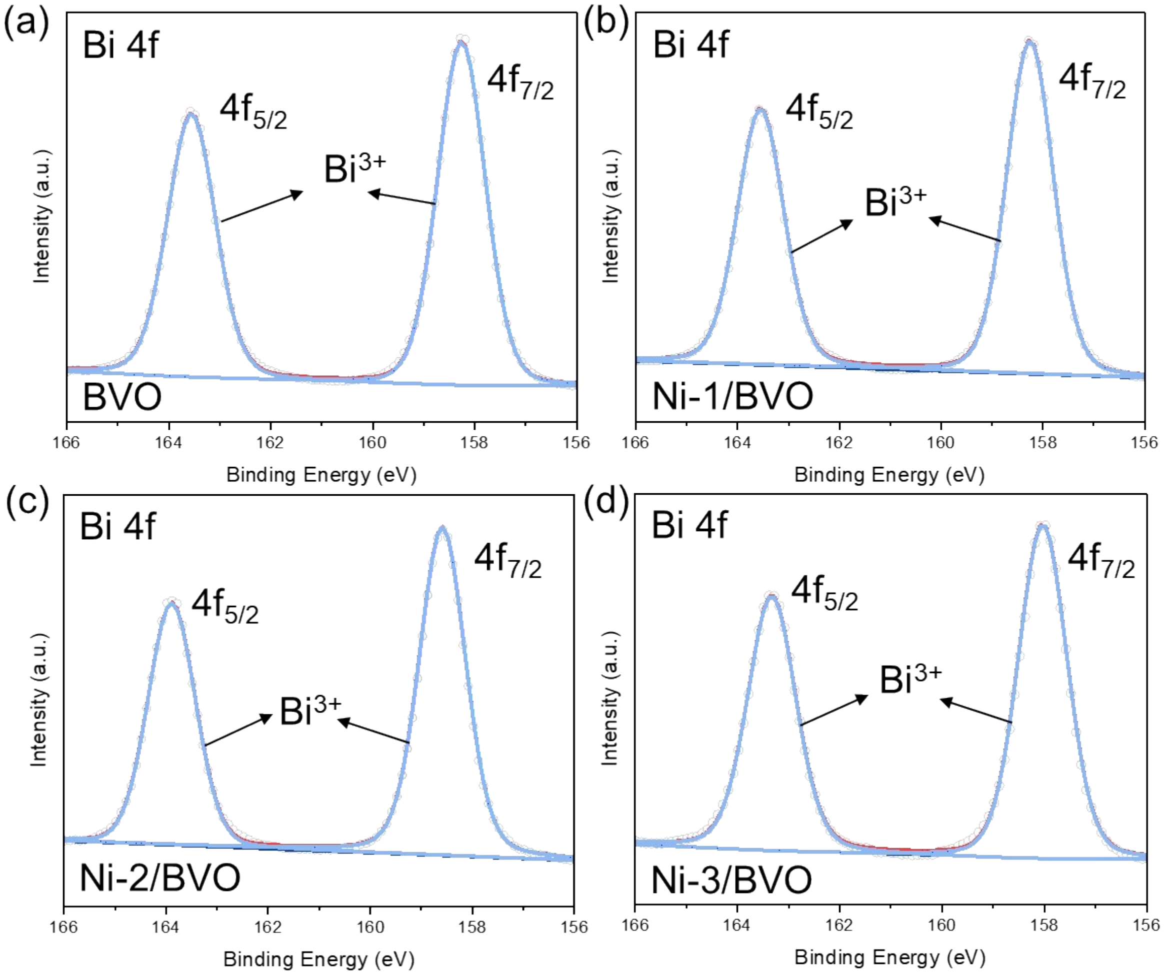

Figure S27. XPS spectra of Bi 4f peaks of (a) BVO, (b) NO-1/BVO, (c) NO-2/BVO, and (d) NO-3/BVO.

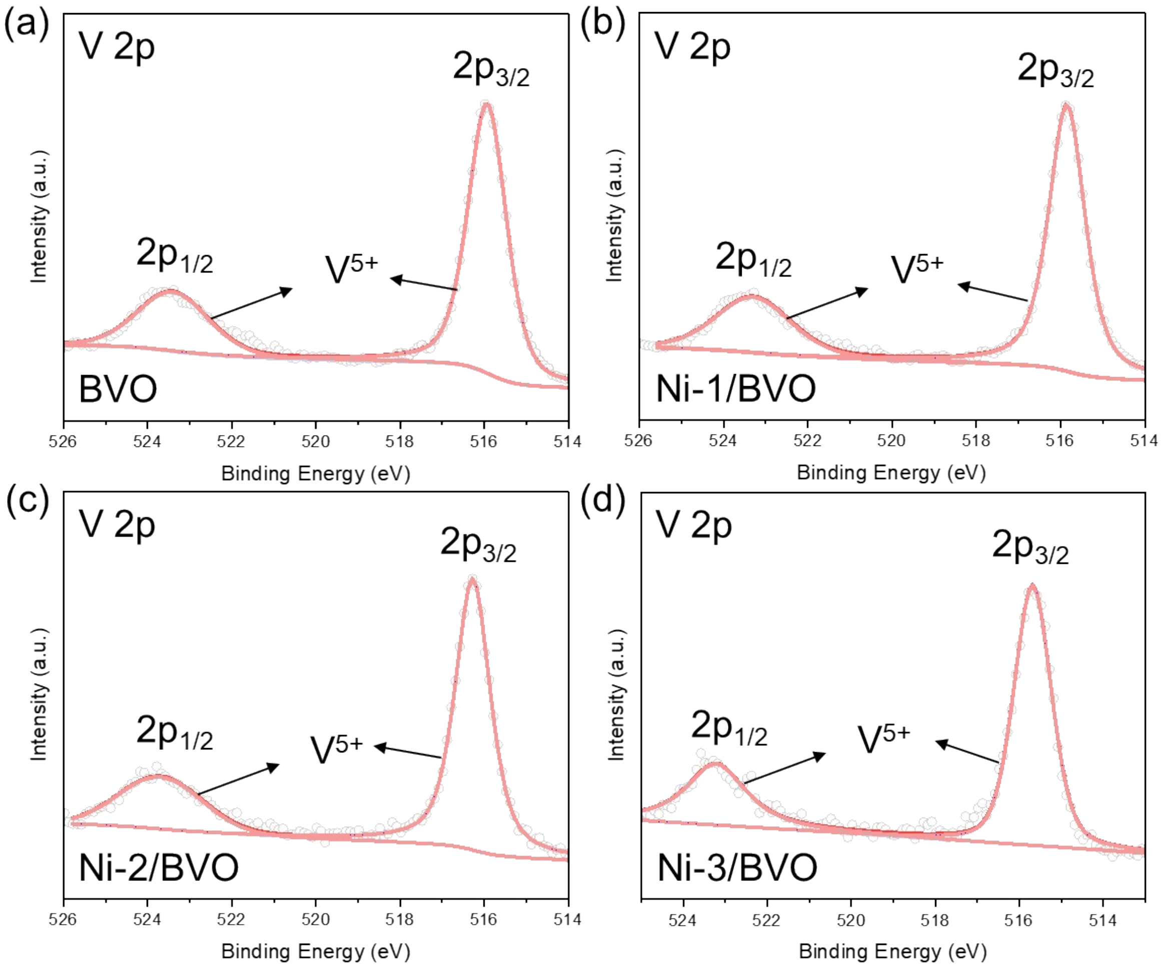

Figure S28. XPS spectra of V 2p peaks of (a) BVO, (b) NO-1/BVO, (c) NO-2/BVO, and (d) NO-3/BVO.

The deconvoluted V 2p spectra show the presence of V^{4+} in BVO, NO-1/BVO, NO-2/BVO, and NO-3/BVO photoanodes (515.7 eV and 522.8 eV for V^{4+} 2p3/2 and V^{4+} 2p1/2, respectively), while all the photoanodes show the peaks located at 516.5 eV and 524.1 eV, which are ascribed to V^{5+} 2p3/2 and V^{5+} 2p1/2 spin-orbit splits, respectively.

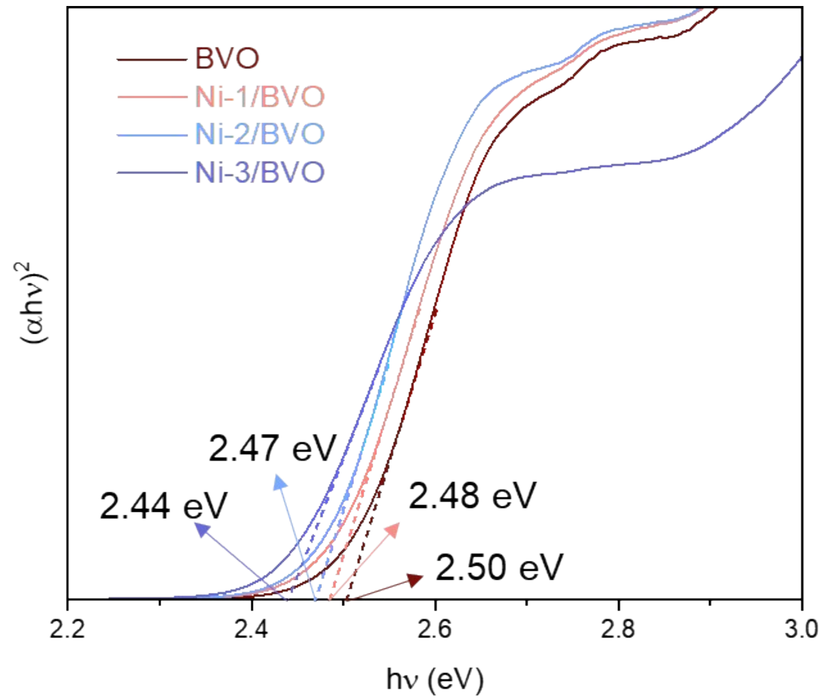

Figure S29. Tauc plot corresponding to UV-Vis absorption spectra of NO-*x*/BVO (*x*=1, 2 and 3) and BVO.

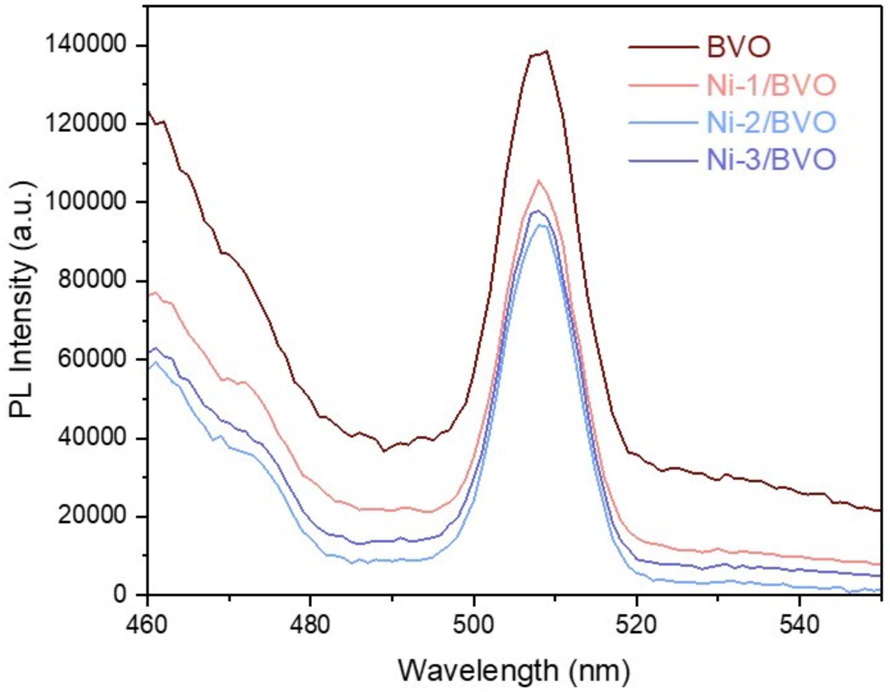

Figure S30. PL spectra of BVO and NO-*x*/BVO (*x* =1, 2 and 3).

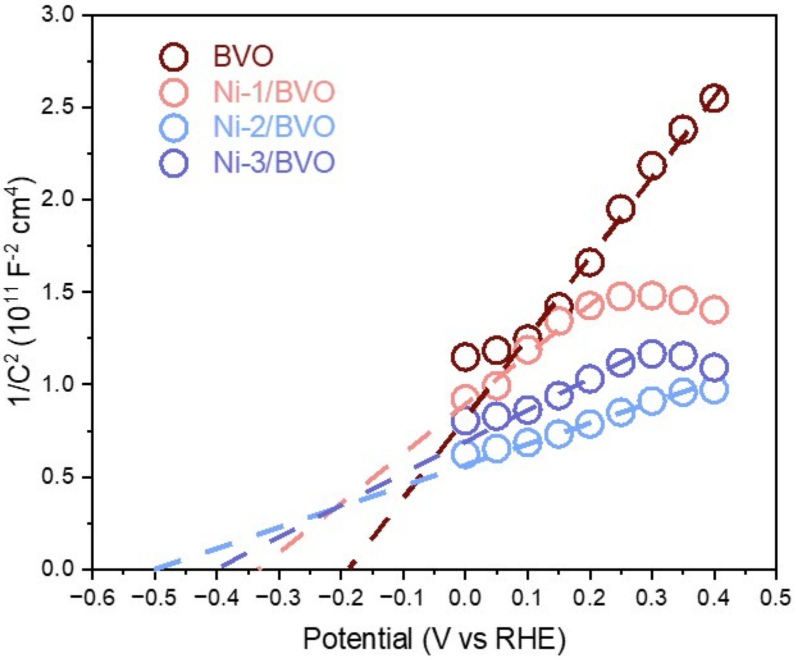

Figure S31. Mott-Schottky plots of the BVO, NO-1/BVO, NO-2/BVO, and NO-3/BVO photoelectrodes in 10 mM HMF with 1 M KOH (pH=13).

E_{fb} values of -0.18, -0.32, -0.40, and -0.49 V vs. RHE for BVO, NO-1/BVO, NO-2/BVO, and NO-3/BVO, respectively.

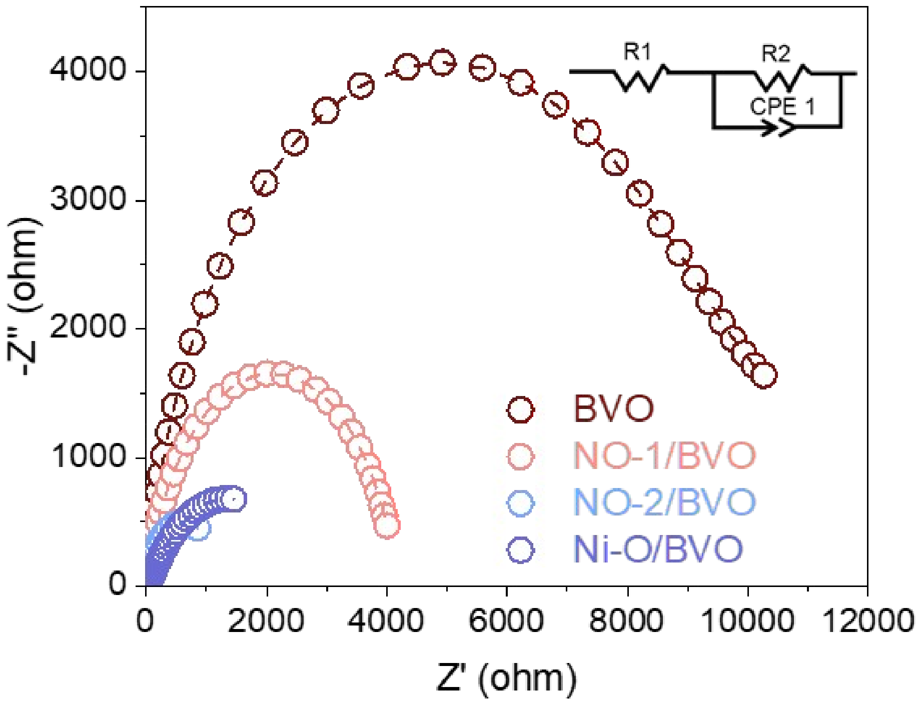

Figure S32. Nyquist plots of BVO and NO-*x*/BVO (*x* =1, 2 and 3).

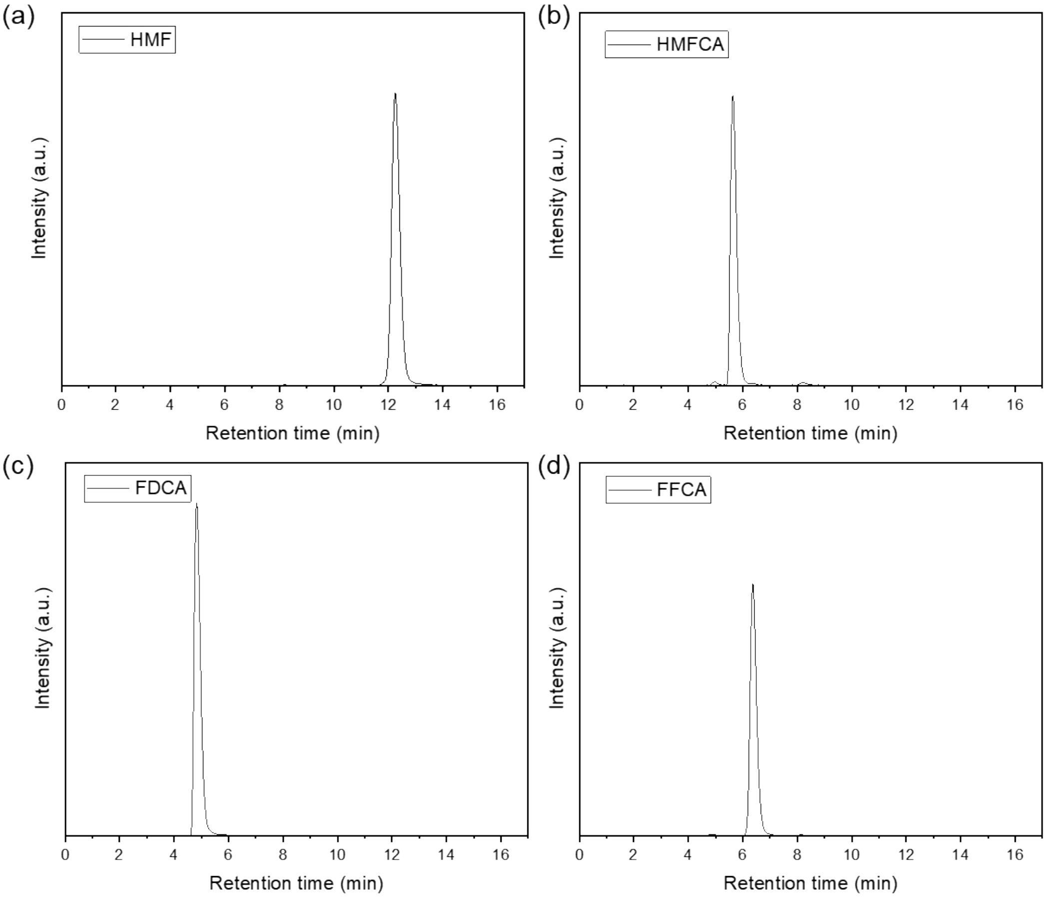

Figure S33. Retention time of (a) HMF, (b) HMFCA, (c) FDCA, and (d) FFCA standard sample by HPLC

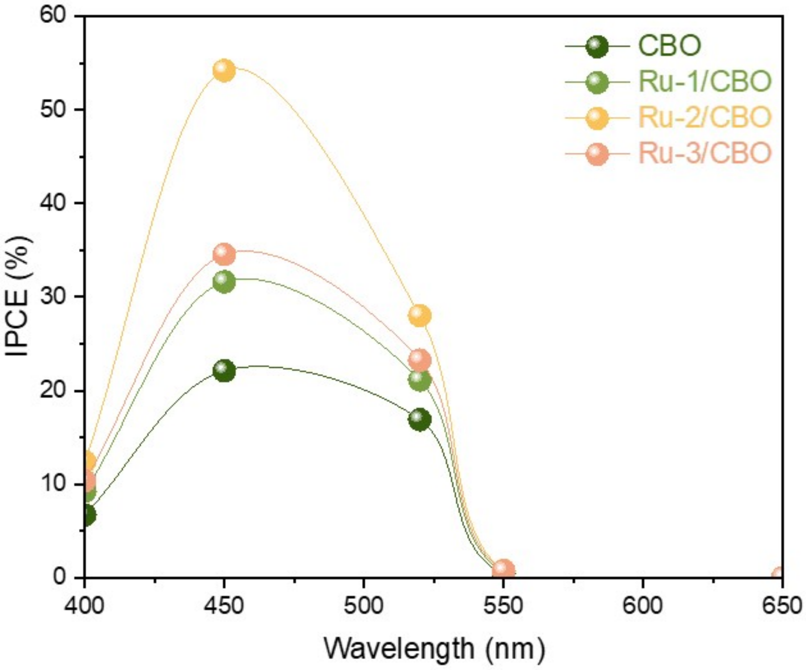

Figure S34. Wavelength-dependent IPCE of different photocathodes.

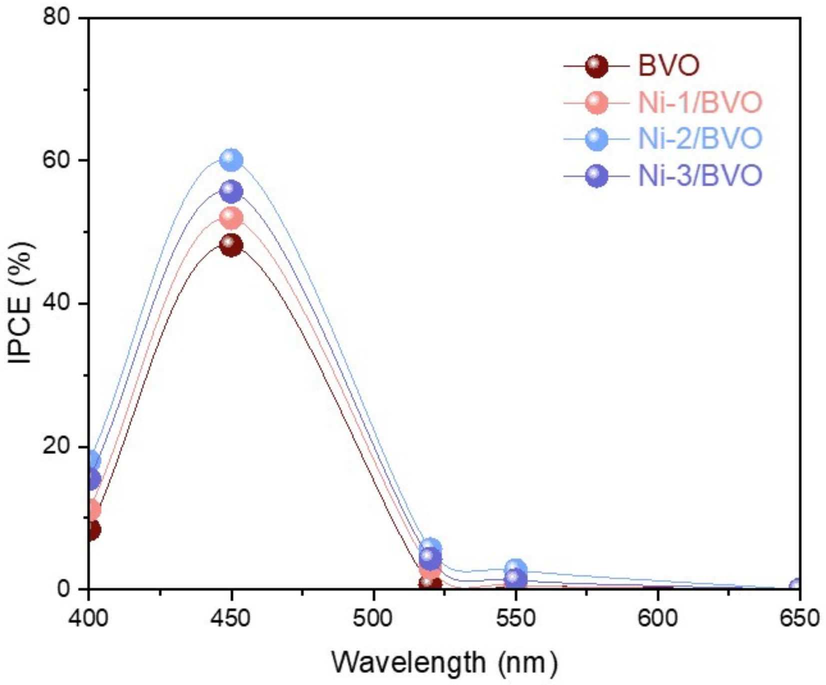

Figure S35. Wavelength-dependent IPCE of different photoanodes.

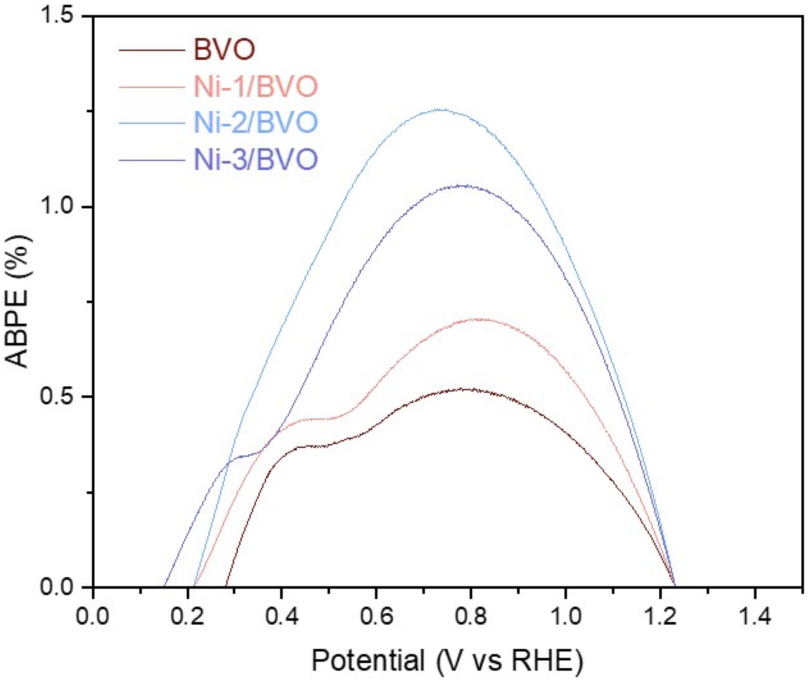

Figure S36. Measured ABPE of different photoanodes.

The NiOOH co-catalyst significantly enhances the solar energy conversion efficiency of BVO. The ABPE value for Ni-2/BVO was measured at 1.25% (0.73 V vs. RHE), which is substantially higher than that of Ni-1/BVO (0.70%, 0.80 V vs. RHE) and Ni-3/BVO (1.06%, 0.78 V vs. RHE). The optimal potential for achieving the maximum ABPE decreased gradually, with Ni-2/BVO showing an ABPE more than 2.4 times greater than that of pure BVO (0.52%, 0.80 V vs. RHE).

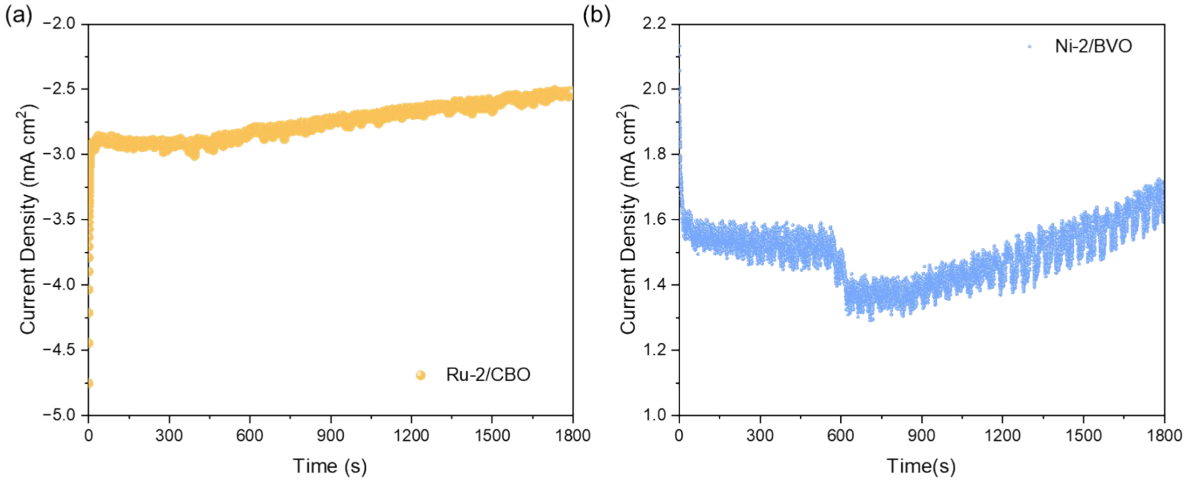

Figure S37. I-t plots of (a) Ru-2/CBO photocathodes under illumination at 0.2 V vs. RHE, and (b) Ni-2/CBO photoanodes under illumination at 1.2 V vs. RHE. All measurements were conducted in 1 M KOH containing 10 mM HMF solution (pH = 13).

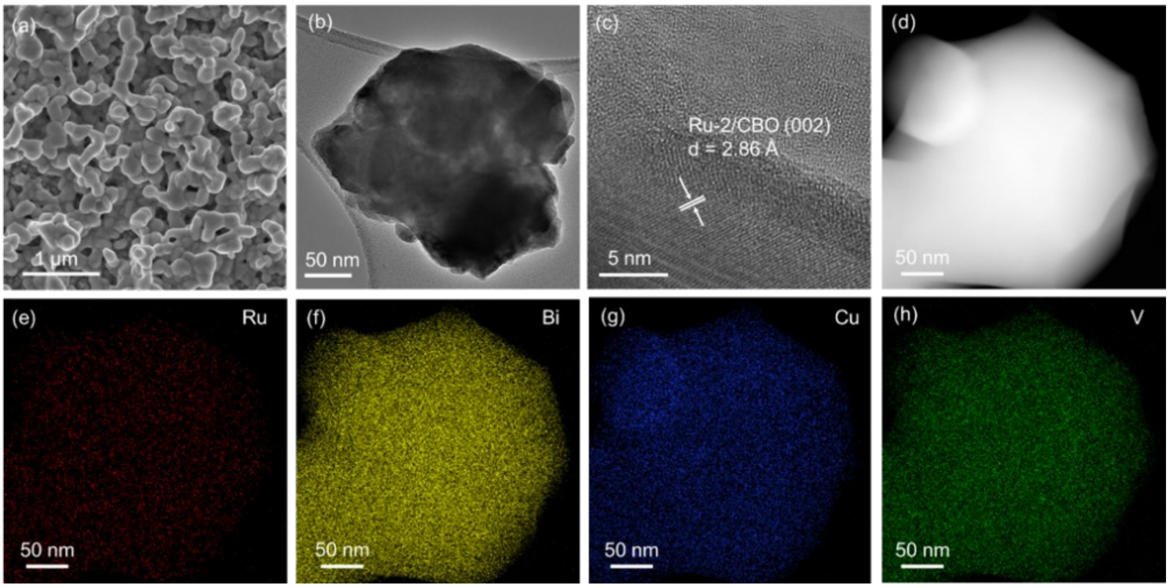

Figure S38. Ru-2/CBO after the stability test. (a) SEM image, (b) HADDF image, (c) HR-TEM image, (d) HADDF, and the corresponding (e-h) EDS mapping of Ru-2/CBO after stability test.

Ru-2/CBO, after the stability test, exhibited nanoporous morphology. However, the particles were fused and grown, forming worm-like morphology, which improved the interconnectivity of the particles and eventually led to the formation of crystalline Ru-2/CBO.

The lattice spacing of 0.286 nm agrees with the interplanar separation of the (002) face of CBO. Notably, the Ru-2/CBO exhibited uniform coverage, including a homogeneous distribution of Ru, Cu, Bi, and V elements.

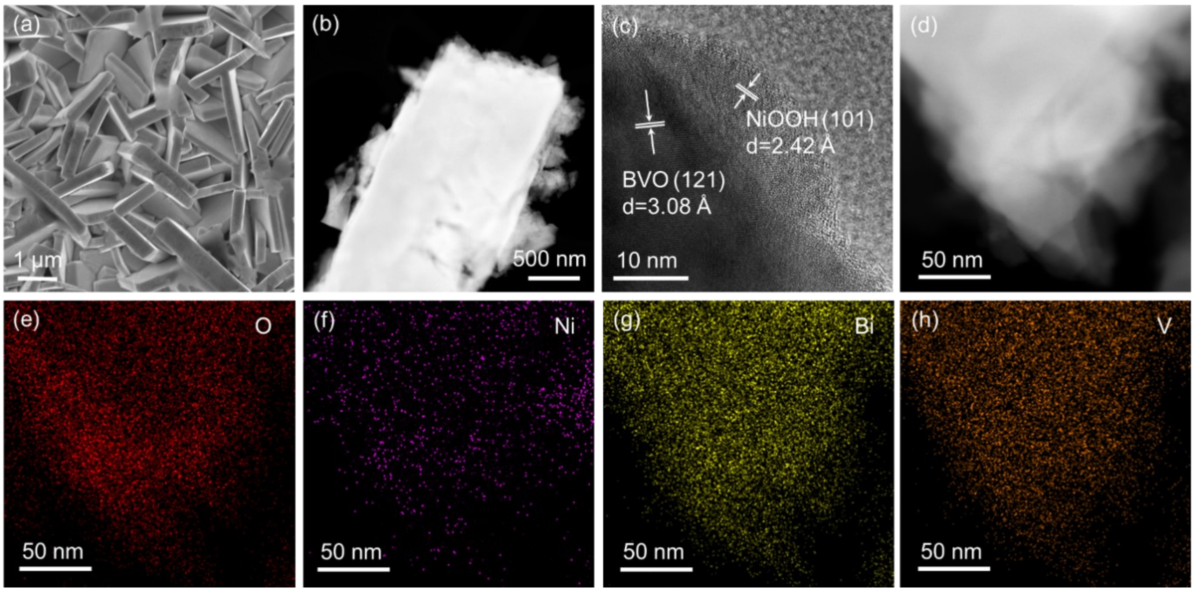

Figure S39. NO-2/BVO. (a) SEM image, (b) STEM image, (c) HR-TEM image, (d) HADDF, and the corresponding (e-h) EDS mapping of NO-2/BVO after stability test.

NO-2/BVO consists of nanoplates with a thickness of around 150 nm after the recycle reaction. The HADDF-STEM image of the NO-2/BVO photoanode shows that the BVO is homogeneously decorated by numerous NiOOH layers. TEM was performed to provide more detailed information on the surface-loaded NiOOH. The HRTEM image of the NO-2/BVO photoanode further revealed that the surface NiOOH preferentially exposed the (101) plane of NiOOH. The lattice fringe of 0.308 nm can be assigned to BVO (121). The STEM mapping after the stability test of the NO-2/BVO photoelectrode showed that the Ni, O, Bi, and V elements were still evenly distributed in the catalyst.

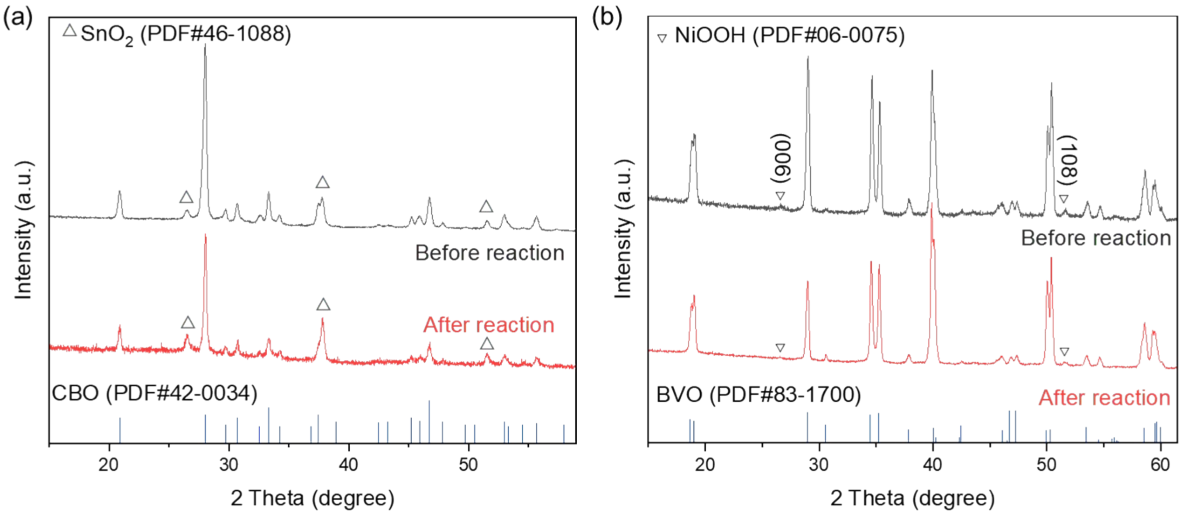

Figure S40. XRD pattern of (a) Ru-2/CBO and (b) NO-2/BVO after stability test.

The Ru-2/CBO photocathode and NO-2/BVO photoanodes after the reaction produced an XRD diffractogram that generally matched the photoelectrodes before the reaction.

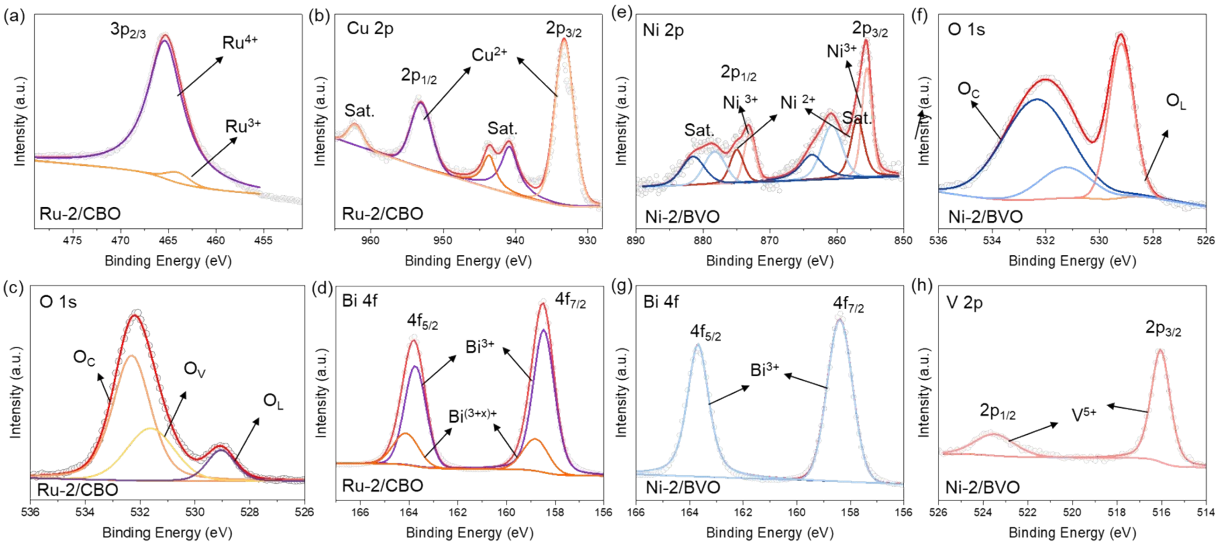

Figure S41. XPS spectra of (a-d) Ru-2/CBO and (e-h) NO-2/BVO after stability test.

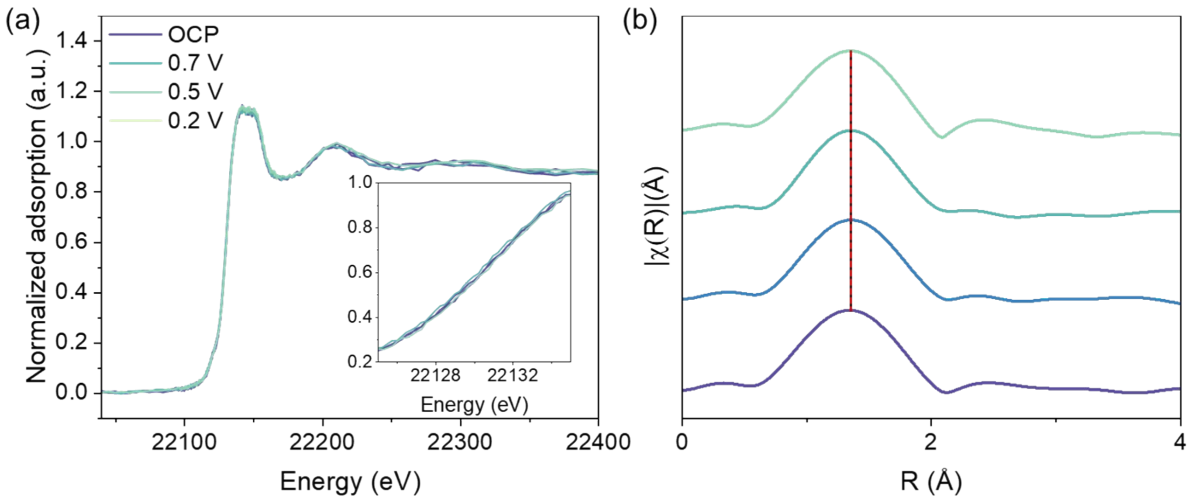

Figure S42. (a) *In-situ* Ru K-edge XANES of Ru-2/CBO under EC HMF oxidation. (b) FT-EXAFS spectra of Ru-2/CBO under EC HMF oxidation.

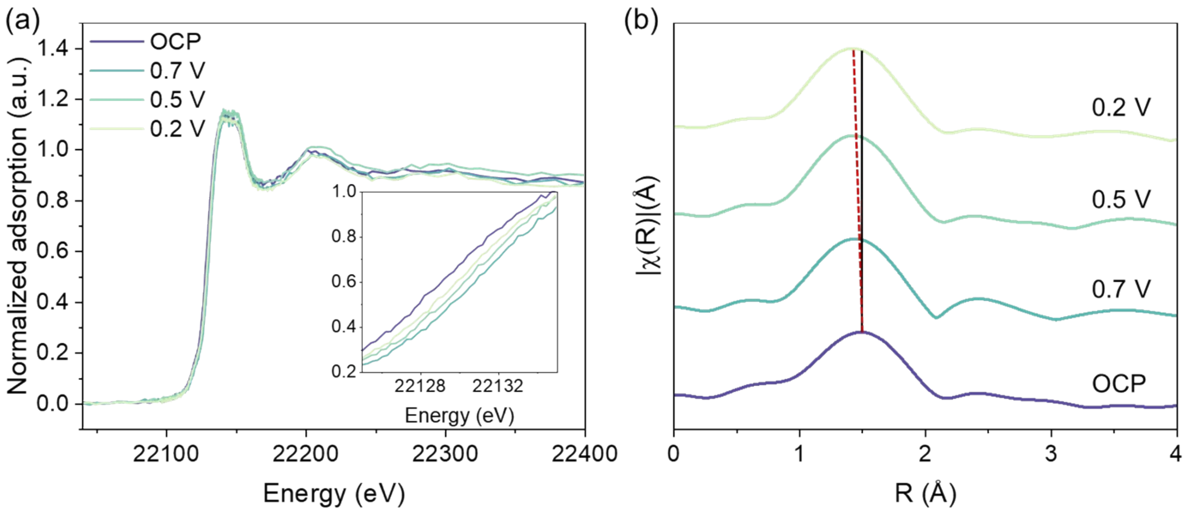

Figure S43. (a) *In-situ* Ru K-edge XANES of Ru-2/CBO under PEC HMF oxidation. (b) FT-EXAFS spectra of Ru-2/CBO under PEC HMF oxidation.

2. Supporting Table

Table S1. DFT calculation of the formation energy of Ru doping at different sites.

	Ru at Cu-site	Ru at Bi-site
Formation energy (eV)	0.507	1.162

Table S2. Bader charges analysis for Ru doping at different sites.

	Pristine	Ru at Cu-site
O	-0.932 *e*	-1.065 *e*
Cu	+0.966 *e*	+0.872 *e*
Bi	+1.654 *e*	+1.65 *e*
Ru	-	+1.241 *e*

Table S3. EXAFS fitting parameters at the Ru K-edge for Ru-2/CBO.

	Bond	N	R (Å)	σ^2	ΔE (eV)	R-factor (%)
Ru foil	Ru-Ru	4.84±0.81	2.73±0.07	0.001	3.34±1.04	0.9
RuO_2	Ru-O	2.32±0.28	1.94±0.02	0.002	2.69±1.25	1.1
	Ru-Ru	4.50±2.42	3.11±0.05	0.005	2.69±1.25	1.1
Ru-2/CBO	Ru-O	2.38±0.24	1.94 ±0.07	0.002	1.92±1.21	0.4
	Ru-Cu	0.92±0.26	2.76±0.02	0.005	1.09±0.49	2.2

Table S4. Summary of the carrier density for CBO and Ru-*x*/CBO (*x*=1, 2 and 3).

Cathode	Nd (cm^{-3})
CBO	3.3×10^{19}
Ru-1/CBO	4.5×10^{19}
Ru-2/CBO	1.4×10^{20}
Ru-3/CBO	9.2×10^{19}

Table S5. Summary of the carrier density for BVO and NO-*x*/BVO (*x*=1, 2, and 3).

Anode	N_d (cm^{-3})
BVO	4.0×10^{18}
NO-1/BVO	5.9×10^{18}
NO-2/BVO	1.8×10^{19}
NO-3/BVO	1.2×10^{19}

Table S6. Comparison of PEC HMF oxidation to HMFCA across different (photo)anodes.

System	FE_{HMFCA}	Select.	Bias Voltage	Current	pH	Ref.
NO-2/BVO Photoanode	75.8%	76.1%	0.89 V vs. RHE	0.68 mA cm^{-2}	13	This work
Ru-2/CBO Photocathode	77.6%	75.2%	0.89 V vs. RHE	0.68 mA cm^{-2}	13	This work
Fe_2O_3	-	83.9%	1.23 V vs. RHE	0.75 mA cm^{-2}	12	[4]
Ag-Co(OH)$_2$	＜15%	91.3%	1.1 V vs. RHE	1 mA cm^{-2}	-	[5]
Cu_2O-CF	84%	100%	0.11 V vs. RHE	10 mA cm^{-2}	13	[6]
CoO_xH_y	88.7%	96%	1.1 V vs. RHE	＜0.25 mA cm^{-2}	13	[7]
CuO on Cu foam	-	＜ 60%	1.2 V vs. RHE	1 mA cm^{-2}	13	[8]

Reference

1. S. Wu, X. Yu, J. Zhang, Y. Zhang, Y. Zhu and M. Zhu, *Chemical Engineering Journal*, 2021, **411**, 128555.
2. B. Zhang, X. Huang, Y. Zhang, G. Lu, L. Chou and Y. Bi, *Angew. Chem. Int. Ed.*, 2020, **59**, 18990-18995.
3. J.-B. Pan, B.-H. Wang, J.-B. Wang, H.-Z. Ding, W. Zhou, X. Liu, J.-R. Zhang, S. Shen, J.-K. Guo, L. Chen, C.-T. Au, L.-L. Jiang and S.-F. Yin, *Angew. Chem. Int. Ed.*, 2021, **60**, 1433-1440.
4. A. Kawde, M. Sayed, Q. Shi, J. Uhlig, T. Pullerits and R. Hatti-Kaul, *Catalysts*, 2021, **11**, 969.
5. P. Zhou, X. Lv, H. Huang, B. Cheng, H. Zhan, Y. Lu, T. Frauenheim, S. Wang and Y. Zou, *Advanced Materials*, 2024, **36**, 2312402.
6. H. Chen, C. Ding, Y. Li, L. Wang, C. Li and J. He, *Journal of Environmental Chemical Engineering*, 2024, **12**, 112614.
7. X. Deng, G.-Y. Xu, Y.-J. Zhang, L. Wang, J. Zhang, J.-F. Li, X.-Z. Fu and J.-L. Luo, *Angewandte Chemie International Edition*, 2021, **60**, 20535-20542.
8. X. Li, W. Zhu, F. Yue, H. Pang, C. Wang, D. Wang, Y. Lu and C. Yang, *Applied Catalysis B: Environment and Energy*, 2024, **358**, 124418.